fibers

MDPI

Article

Harnessing the Unique Nature of Evanescent Waves: Optimizing FOEW LSPR Sensors with Absorption-Focused Nanoparticle Design

Omar Awad [1,*], AbdulRahman Ghannoum [2,*] and Patricia Nieva [1,*]

[1] Department of Mechanical Engineering, University of Waterloo, 200 University Avenue West, Waterloo, ON N2L 3G1, Canada
[2] Department of Chemical Engineering, Qatar University, Doha P.O. Box 2713, Qatar
* Correspondence: omar.awad@uwaterloo.ca (O.A.); aghannoum@qu.edu.qa (A.G.); pnieva@uwaterloo.ca (P.N.)

Abstract: This work presents a novel and comprehensive framework for optimizing fiber optic evanescent wave (FOEW) localized surface plasmon resonance (LSPR) sensors by investigating the unique interaction between evanescent waves and plasmonic nanoparticles. Unlike propagating light, the evanescent wave is a localized, non-propagating field that interacts exclusively with absorbing media near the fiber surface. This characteristic highlights the importance of prioritizing nanoparticle absorption over total extinction in FOEW sensor design. The optical response of silver nanoparticles was modeled across a size range of 10–100 nm, showing that absorption increases with particle number. Among the sizes tested, 30 nm silver nanoparticles exhibited the highest absorption efficiency, which was confirmed experimentally. An analytical adsorption kinetics model based on diffusion transport further predicted that smaller nanoparticles yield higher surface coverage, a result validated through atomic force microscopy (AFM) and scanning electron microscopy (SEM) imaging. Refractive index (RI) sensitivity tests conducted on sensors fabricated with 10 nm, 20 nm, and 30 nm silver nanoparticles revealed that while smaller nanoparticles produced higher initial absorption due to greater surface density, the 30 nm particles ultimately provided superior RI sensitivity due to their enhanced absorption efficiency. These findings underscore the significance of absorption-centered nanoparticle design in maximizing FOEW LSPR sensor performance.

Keywords: localized surface plasmon resonance; nanoparticles; optical fiber sensor; evanescent wave sensors; coreless fiber; diffusion transport kinetics

check for updates

Academic Editors: Martin J. D. Clift and Paulo Caldas

Received: 1 March 2025
Revised: 8 June 2025
Accepted: 13 June 2025
Published: 17 June 2025

Citation: Awad, O.; Ghannoum, A.; Nieva, P. Harnessing the Unique Nature of Evanescent Waves: Optimizing FOEW LSPR Sensors with Absorption-Focused Nanoparticle Design. *Fibers* **2025**, *13*, 81. https://doi.org/10.3390/fib13060081

Copyright: © 2025 by the authors. Licensee MDPI, Basel, Switzerland. This article is an open access article distributed under the terms and conditions of the Creative Commons Attribution (CC BY) license (https://creativecommons.org/licenses/by/4.0/).

1. Introduction

Fiber optic evanescent wave (FOEW) sensors have attracted significant attention for biological, environmental, and chemical applications [1–4]. FOEW sensors operate on the principle of total internal reflection (TIR) within an optical fiber, where electromagnetic rays are confined to the core due to a lower refractive index in the surrounding cladding. However, the electric field associated with these electromagnetic rays extends into the material surrounding the core. This electric field is called the evanescent wave, and its magnitude decays exponentially with the radial distance from the core's interface [5]. In an absorbing medium, molecules near the core's surface (i.e., within the penetration depth of the evanescent wave) interact with the evanescent wave, absorbing its energy [6]. This absorption attenuates the guided light via attenuated total reflection (ATR), which can

be monitored to extract information about the medium. Detecting and analyzing this attenuation provides accurate information about the properties of the absorbing medium.

FOEW sensor performance can be enhanced through modifications to the sensing region. Various physical modifications to the fiber, such as tapering [7], bending [8,9], etching [10], grinding [11], coating [12], grating [13], and many other techniques have been shown to enhance FOEW sensor sensitivity. These techniques increase the intensity and/or penetration depth of the evanescent field, leading to a significantly increased interaction with the medium, thus improving the sensors' performance.

Combined with the qualities of localized surface plasmon resonance (LSPR) sensing, FOEW sensors have emerged as a leading approach for many sensing applications, especially in biosensing, due to their inherent qualities such as ease of fabrication and implementation, high sensitivity, low limit of detection (LOD), real-time monitoring, and good biochemical compatibility. Integrating LSPR with FOEW sensors enhances sensitivity and supports point-of-care applications [14–19].

In LSPR sensors, the size, shape, material, and refractive index of the medium where the nanoparticles exist affect their LSPR wavelength [18,20–25]. When resonance conditions are met, the cloud of electrons around the metal nanoparticles starts oscillating, resulting in light extinction, mainly due to a combination of both absorption and scattering [26,27]. Since evanescent waves are non-propagating, they are not subject to scattering. Consequently, light traveling in an uncladded fiber placed in a purely scattering medium would retain its total internal reflection (TIR) [28]. Therefore, optimizing nanoparticles based solely on their total extinction (i.e., the sum of absorption and scattering) may be misleading in FOEW LSPR sensors. It is important to deconvolute the nanoparticles' light extinction into scattering and absorption, and optimize the nanoparticles to maximize their absorption efficiency instead. In addition, when fabricating FOEW LSPR sensors using self-assembly, the kinetics of nanoparticle adsorption should also be investigated and optimized to attain uniform surface coverage and maximum nanoparticle surface density on the sensing region [29,30].

Models found in the literature used to determine the effect of nanoparticle size on the performance of FOEW LSPR sensors usually only consider the nanoparticle's extinction. Sai et al. presented an analytical model to determine the signal of FOEW LSPR sensors as a function of the extinction coefficient of the nanoparticles [31]. The model was not verified against experimental results, but instead, it was used to highlight the parameters that influence the sensor response. Although the model is very useful, FOEW sensors are not affected by a scattering medium, as stated earlier. Therefore, strictly using the absorption coefficient of the medium instead of the extinction coefficient would better represent the sensor's response.

M.H. Tu et al. studied the effect of immobilizing 13 nm, 20 nm, 40 nm, and 60 nm spherical gold nanoparticles on an optical fiber core functionalized with APTMS [32]. The adsorption time, referred to as dip coating, for each size, was noticed to be longer for larger particles, which also resulted in lower surface densities. These findings are consistent with trends observed in our study and discussed later. However, the author in [32] utilized different adsorption times for each size. The impact of nanoparticle size on surface density for equivalent adsorption times was not investigated, and the concentrations of the colloidal solutions were not disclosed. The lower surface density was attributed to the stronger electrostatic forces experienced by the larger particles, due to the higher surface concentration of citrate ions, consistent with the findings of M. Oćwieja et al. [29].

However, M. Oćwieja et al. demonstrated that the higher surface density for smaller nanoparticles is due to the kinetics of the adsorption, which are controlled by the diffusion transport process [30]. This may explain why the adsorption time varied with nanoparticle

size in [32], and larger nanoparticles required more time for the surface to saturate. M.H. Tu et al. also concluded that "The increase of the diameter of gold nanospheres leads to a higher sensitivity of the LSPR sensor when it is subjected to refractive index changes of the surrounding medium". While this trend was observed for the specific sizes in [32], it does not universally apply, as the same work highlights in different sections. A study by Hun Lee et al. [33] found that LSPR optical fiber sensors fabricated with smaller gold nanoparticles exhibit higher sensitivities when compared to larger nanoparticles for the same coverage area. Hence, higher sensitivities can be attributed to a combination of a higher absorption coefficient and higher surface coverage and not simply the nanoparticle size.

In a recent work by Masheli et al. [34], the authors examined the LSPR behavior of silver nanoparticles in an absorbent medium. They introduced the reflectance spectral correction (RSC) and extinction spectral decomposition (ESD) methods, which allowed them to separate the reflection, absorption, and scattering components of the resonance signal. Their results lead them to conclude that at LSPR, the scattering effects vanished, leaving absorption as the dominant resonance mechanism. We posit that the disappearance of the scattering effect, as observed in their work, is due to the nature of the evanescent wave explained earlier. This phenomenon explains why scattering plays a negligible role in FOEW LSPR sensors, making absorption-driven designs critical for optimizing sensor performance.

While prior studies have provided valuable insights, two critical gaps remain in the literature. First, most optical models rely on the extinction coefficient of nanoparticles, overlooking the fact that scattering does not contribute to FOEW sensing. This can lead to inaccurate predictions of sensor performance. Second, although some work has explored the effect of nanoparticle size on surface coverage, few have investigated how adsorption kinetics and size-dependent absorption efficiency together influence sensor response, particularly in FOEW LSPR systems fabricated via self-assembly.

To address these gaps, this study investigates the dual role of absorption and adsorption in FOEW LSPR sensor performance fabricated via the self-assembly of silver spherical nanoparticles. We derive and experimentally validate an analytical model that predicts sensor response as a function of nanoparticle size, shape, material, and adsorption rate. By decoupling absorption from scattering and systematically analyzing adsorption kinetics across particle sizes, this work provides a more accurate and predictive framework for designing high-performance FOEW LSPR sensors.

2. Modeling Methodology

The modeling presented in this paper is performed in three main steps. First, a numerical model is used to calculate the nanoparticle LSPR absorption of light. Subsequently, an analytical model is developed to determine the adsorption kinetics of nanoparticles on the fiber's surface. Finally, an analytical approach is used to formulate the signal response of the FOEW sensor, incorporating the results from the first two models.

2.1. Numerical Nanoparticle LSPR Absorption Model

The LSPR effect on metal nanoparticles can be captured using the generalized Mie theory, which is essentially a solution to Maxwell's equations that determines the extinction (absorption plus elastic scattering) of light due to the LSPR of spherical nanoparticles [35]. The extinction spectrum of a spherical nanoparticle using Mie theory is described as follows:

$$C_{ext} = A \times B \tag{1}$$

$$A = \frac{24\pi^2 N r_{np}^3 \varepsilon_2^{3/2}}{\lambda \ln(10)} \tag{2}$$

$$B = \frac{\varepsilon_i(\lambda)}{(\varepsilon_r(\lambda) + 2\varepsilon_2)^2 + \varepsilon_i(\lambda)^2} \tag{3}$$

where N is the electron density of the nanoparticles, r_{np} is the nanoparticle radius, ε_2 is the medium's dielectric constant, λ is the wavelength of the incident light, and ε_i and ε_r are the imaginary and real parts of the material's dielectric function, respectively.

The DGTD 3D electromagnetic simulation module by ANSYS 2022 R1 Lumerical Inc. (Canonsburg, PA, USA) was used to model the interaction of light with a single silver nanoparticle, followed by an analysis of how increasing the number of nanoparticles affects light extinction. While the simulation framework is applicable to a range of plasmonic materials, silver was selected due to its superior sensitivity, narrower LSPR linewidths, and to maintain clarity and focus throughout this extended study. The DGTD module numerically solves Mie theory to calculate the absorption and scattering characteristics of the simulated nanoparticle. The initial setup consisted of a single silver nanoparticle placed in a medium with a refractive index of 1.34 to simulate an aqueous environment (see Figure 1).

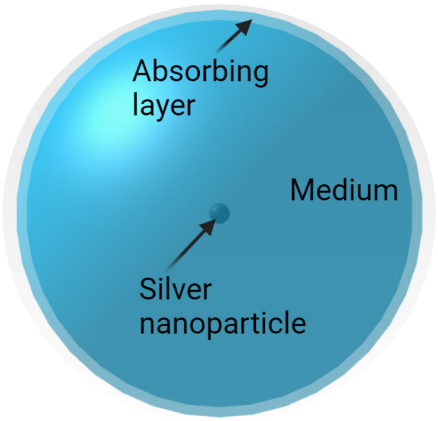


Figure 1. Simulation model of a single silver nanoparticle immersed in water, constructed using DGTD module by ANSYS 2022 h R1 Lumerical Inc. to evaluate localized surface plasmon resonance (LSPR) characteristics in a homogeneous dielectric medium.

As shown in Figure 1, the boundary around the medium is defined as the absorbing layer and the surface of the absorbing layer is set to be the source of the electromagnetic wave. A frequency monitor is used to calculate the extinction of light due to the interaction with the nanoparticle, which is placed on the surface of the absorbing layer as well. This allows the software to separate the extinct light and the light injected by the source. The electromagnetic wave is set as a plane wave with an amplitude of 1 V/m and a wavelength ranging from 350 nm to 750 nm. Generally, LSPR simulations use silver optical properties from Johnson and Christy's (J & C) tabulation, or Palik's 1985 handbook [36]. For this work, the simulations were carried out using both data sets and the results were averaged out.

The simulation was conducted to determine both the scattering cross-section, C_{scat}, and the absorption cross-section, C_{abs}, for individual silver nanoparticles with diameters ranging from 10 to 100 nm, in 10 nm increments. The results were in units of ($A.U.\ m^2$), where $A.U.$ stands for arbitrary unit, and it is a unitless measurement of the optical density. The simulation was conducted in a 1.34 refractive index medium, with light wavelengths ranging from 350 to 750 nm in 10 nm increments. The extinction cross-section C_{ext} was computed by adding C_{scat} and C_{abs}. A plot of the peak LSPR C_{ext}, C_{scat}, and C_{abs} generated for each nanoparticle size is shown in Figure 2. From the results, we can see

how both scattering and absorption contribute to LSPR with different magnitudes, which is expected [20].

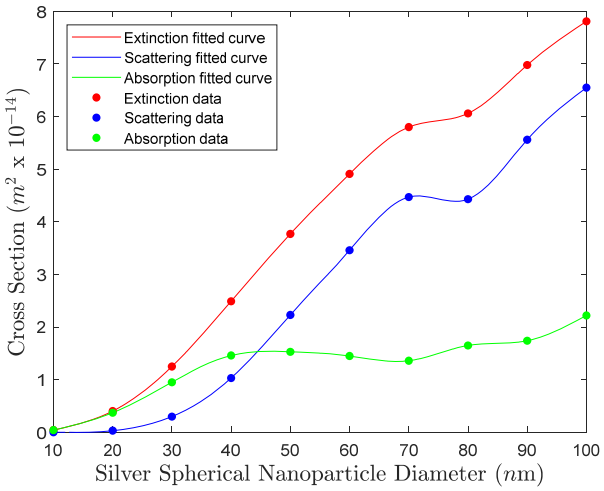


Figure 2. Maximum LSPR cross-section peaks for silver nanoparticles ranging in size from 10 nm to 100 nm, each at its respective resonance wavelength in a medium with a refractive index of 1.34. A cubic spline fit interpolates the simulation data.

The results in Figure 2 show that generally larger nanoparticles have a higher extinction, scattering, and absorption cross-section, with some exceptions that mainly result from averaging out J & C [37] and Palik's [38] data. This is expected since the cross-section parameter depends on the nanoparticle's cross-sectional area, which increases with particle size. However, in the case of evanescent fields, being non-propagating, the dimensionless efficiencies (Q_{ext}, Q_{scat}, and Q_{abs}) become the more pertinent parameters for evaluating nanoparticle optical behavior. These efficiencies are obtained by dividing the computed cross-sections by the geometric cross-sectional area of the nanoparticle. This was carried out for the same range of silver nanoparticle sizes and used to generate Figure 3.

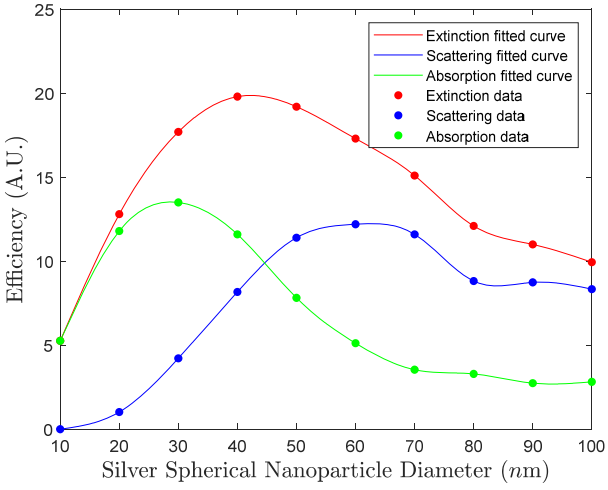


Figure 3. Maximum LSPR efficiency peaks for silver nanoparticles ranging in size from 10 nm to 100 nm, each at their respective resonance wavelength in a medium with a refractive index of 1.34. A cubic spline fit interpolates the simulation data.

Figure 3 illustrates the variation of Q_{ext}, Q_{scat}, and Q_{abs} with nanoparticle size, though no clear or consistent trend is observed. Notably, the absorption efficiency increases as the particle size grows from 10 nm to 30 nm, peaking at 30 nm, after which it declines. Consequently, the 30 nm nanoparticle exhibits the highest absorption efficiency among the

sizes considered. In contrast, Figure 2 shows that the absorption cross-section increases monotonically with particle size, suggesting that larger silver nanoparticles absorb more light. This discrepancy highlights a key distinction: while larger particles absorb more light overall, they do so less efficiently relative to their size. Specifically, Figure 2 favors larger particles for total absorption, whereas Figure 3 identifies 30 nm particles as the most efficient size for light absorption.

To resolve whether a FOEW LSPR sensor should be optimized for absolute absorption (cross-section) or for absorption efficiency, and to assess the role of extinction in evanescent field interactions, we selected the 30 nm and 80 nm nanoparticles for further analysis. These two sizes demonstrate opposite trends, the 80 nm particle has a higher absorption cross-section, whereas the 30 nm particle achieves greater absorption efficiency. Importantly, these two sizes exhibit similar extinction coefficients despite having different absorption efficiencies. This makes them ideal candidates for further analysis to reinforce how absorption, rather than extinction, is the key factor influencing FOEW LSPR sensor performance.

To further investigate why the 30 nm size has the highest efficiency, the expression for the absorption of a spherical particle was considered, which is given by [20]:

$$\alpha_{np} = \frac{8\pi R}{\lambda} Im\left\{\frac{\varepsilon_1 - \varepsilon_2}{\varepsilon_1 + 2\varepsilon_2}\right\} \quad (4)$$

where R is the radius of the nanoparticle, λ is the wavelength of light, Im refers to the imaginary part of the expression between brackets, ε_1 is the dielectric constant of the particle, and ε_2 is the dielectric constant of the surrounding medium. The dielectric constant of the particle, ε_1, is a function of the frequency of light interacting with it.

LSPR occurs at the frequency where $\varepsilon_1 \approx -2\varepsilon_2$, causing the denominator to approach zero and the absorption to spike. The frequency at which this occurs is known as Fröhlich frequency, which depends on the particle size, material, shape, and medium surrounding the particle [20]. Based on Figure 3, it appears that for silver nanoparticles of size $\approx$ 30 nm, the value of the Fröhlich frequency corresponds to the highest imaginary value in Equation (4), which explains why this specific size would exhibit the highest absorption efficiency when compared to other silver nanoparticle sizes.

Further modeling was performed to examine the relationship between Q_{abs} and the number of nanoparticles using silver nanoparticles with diameters equal to 80 nm and 30 nm. The number of nanoparticles was increased arbitrarily to 9, 25, 58, and 89 particles, and the results of the total Q_{abs} at each size was plotted in Figure 4. The results show how the absorption efficiency increases linearly as the number of particles increases. This was repeated for different sizes of nanoparticles and the findings were consistent. The results align with our expectations, as the simulations were conducted with nanoparticles separated by distances greater than their diameter. This spacing ensures that the electric field generated by the LSPR of one nanoparticle does not interfere with neighboring particles, thereby isolating their effects. While the self-assembly process typically results in nanoparticles adsorbing onto the surface in closer proximity, these interactions were excluded from the model to simplify the simulations. It is worth noting that the DGTD module can account for such effects if appropriately configured. However, due to the random nature of the self-assembly process, which will be discussed later, these complexities were not incorporated into our model.

The absorption model findings suggest that nanoparticles of varying sizes, as well as differing shapes and materials, exhibit improved scattering and absorption efficiencies without following a consistent trend, unlike their behavior with respect to scattering and absorption cross-section. Furthermore, the model indicates that the density of nanoparticles in a medium interacting with light affects the overall light absorption. Higher nanopar-

ticle densities contribute to higher light absorption. These results imply that optimizing nanoparticles for high absorption efficiency and maximizing their surface density on the sensing region are key to enhancing the performance of a FOEW LSPR sensor.

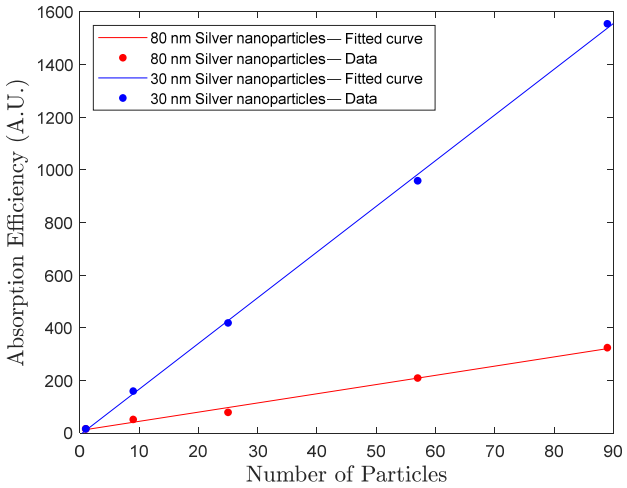


Figure 4. Linear relationship between the peak absorption efficiency (Q_{abs}) and number of nanoparticles calculated for 80 nm and 30 nm diameter silver nanoparticles (straight line fit used to cover all simulation points).

2.2. Analytical Adsorption Kinetics Model

Monolayers of self-assembled silver nanoparticles adsorbed on a substrate treated with cationic polyelectrolyte have been previously studied in the literature [29,30,39,40]. When a substrate treated with a cationic polyelectrolyte (i.e., APTES) is immersed in a nanoparticle colloidal solution, nanoparticles adsorb on the surface due to the difference in charge between the nanoparticles' surface (negative) and the treated substrate (positive) in a process known as self-assembly. The kinetics of this adsorption process are governed by the diffusion transport process [29]. In this case, the surface density is proportional to the immersion time at shorter immersion periods, while at longer periods, the intermolecular repulsion forces come into play, preventing the particles' build-up and resulting in a saturated monolayer surface coverage. The key factors contributing to the repulsion forces between the nanoparticles are the surface charge of the nanoparticle and its size. This can be controlled by surface functionalization of the nanoparticle. The surface density N_s can be described using the following [30]:

$$N_s = 2\sqrt{Dt/\pi}C_b \tag{5}$$

where D, t, and C_b are the diffusion coefficient ($\mu m^2/s$), immersion time (s), and the bulk number concentration, respectively. The surface density is proportional to $\sqrt{t}$. The diffusion coefficient can be calculated using the Stokes–Einstein equation [29]:

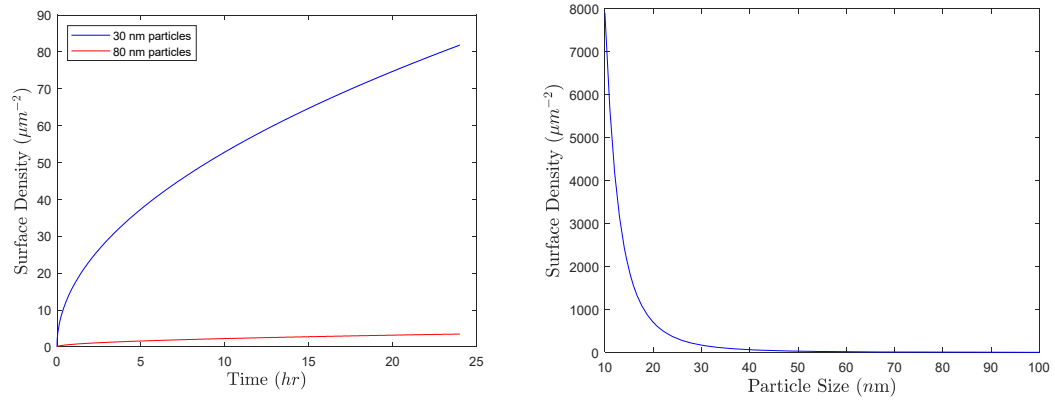
$$D = \frac{k_b T}{3\pi\eta d_H} \tag{6}$$

where d_H is the hydrodynamic diameter of the particle, k_b is the Boltzmann constant, η is the viscosity of the solvent of the colloidal solution, and T is the absolute temperature. For non-spherical nanoparticles, an equivalent diameter can be determined and utilized in the Stokes–Einstein equation to calculate the diffusion coefficient. This diffusion coefficient

can then be applied to the surface density Equation (5). The bulk number concentration C_b is related to the weight concentration c_w through [30]:

$$C_b = \frac{6 \times 10^{-6}}{\pi \, d_{np}^3 \rho_{np}} \, c_w \tag{7}$$

where d_{np} is the average diameter of the particle, ρ_{np} is the density of the particle (i.e., silver), and c_w is the concentration expressed in ppm. According to Equation (5), higher concentrations will result in higher surface density. However, higher surface densities can also be achieved with longer adsorption times. The bulk number concentrations for the particles used were calculated using Equation (7), for a concentration of 20 ppm (which is the concentration of the procured silver nanoparticles used in the experiments section). The diffusion coefficients were calculated using Equation (6). The procured 30 nm particles had a hydrodynamic diameter of 37 nm, while the 80 nm particles had a hydrodynamic diameter of 91 nm. The calculated diffusion coefficient for each particle was then used to determine the surface density using Equation (5) and the results are shown in Figure 5a for 30 nm and 80 nm nanoparticles. Figure 5b shows the surface density for the other sizes.



(**a**) (**b**)

Figure 5. (**a**) Surface density comparison between 30 nm and 80 nm silver nanoparticles adsorbed on the fiber surface after 24 h; (**b**) effect of nanoparticle size on surface coverage density, demonstrating the inverse relationship between size and achievable density.

It can be seen in Figure 5a that after 24 h of adsorption, the 30 nm particles result in a surface density of ~81 particles per μm^2. That is more than 23 times the expected surface density of the 80 nm nanoparticles for the same bulk number concentration and over the same adsorption period, which was only ~3.5 particles per μm^2. Figure 5b shows that smaller particles will always have higher surface density compared to larger particles for the same bulk number concentration and adsorption time. However, it is important to note that once a monolayer of nanoparticles is formed on the surface of the fiber, the repulsion forces will stop any further adsorption. For the two sizes under study, since the results of the model show that using 30 nm nanoparticles will result in higher surface density compared to 80 nm nanoparticles, it is expected that using 30 nm diameter nanoparticles in the fabrication of the sensor will demonstrate improved performance.

2.3. Optical Fiber Sensor Analytical Model

In this work, multimode optical fiber is used due to its larger core diameter, which allows for easier and more efficient light coupling. Additionally, its ability to support multiple spatial modes can be advantageous in certain sensing or imaging applications. Light transmitted through an uncladded fiber immersed in an absorbing medium will result

in an ATR as stated previously. This can be utilized for sensing based on the following expression derived by V. Ruddy et al. for multimode fibers [41]:

$$P(z) = P_0\, e^{(-\gamma z)} \tag{8}$$

where P_0 is the initial power transmitted through the fiber, γ is the evanescent wave absorbing coefficient, and z is the length of the uncladded fiber immersed in the absorbing medium in units of cm. For multimode fibers, γ can be related to the bulk absorption coefficient of a medium α_b using [41]:

$$\gamma = r\alpha_b \tag{9}$$

where r is the fraction of power outside the core and can be calculated from the following [41]:

$$r = \frac{4\sqrt{2}}{3V} \tag{10}$$

where V is the normalized frequency parameter of the fiber given by the following [41,42]:

$$V = \left(\frac{2\pi r_f}{\lambda}\right) NA \tag{11}$$

$$NA = \sqrt{n_{core}^2 - n_{clad}^2} \tag{12}$$

The normalized frequency parameter determines the number of modes supported in a multimode fiber [42]. r_f is the core radius, and NA is the numerical aperture in which light of wavelength λ is propagating. n is the refractive index of the material. Higher numerical aperture (NA) fibers confine light more tightly within the core, producing a more intense but shallower evanescent wave. This makes them well-suited for interactions occurring near the fiber surface. Conversely, lower NA fibers produce an evanescent wave with greater penetration depth into the surrounding medium, enhancing sensitivity to analytes located farther from the surface. Combining Equations (8)–(10), the final absorbance of the evanescent wave affecting the total power transmitted through the fiber is as follows:

$$A = \frac{4\sqrt{2}}{3V}\,\frac{\alpha_b\, z}{2.303} \tag{13}$$

The bulk absorption coefficient of a medium α has units of $(A.U.\ cm^{-1})$. To represent the absorbance of an LSPR evanescent wave optical fiber sensor with nanoparticles adsorbed on the core's surface, Equation (13) is modified by replacing the absorption coefficient of the medium α with the absorption efficiency of the nanoparticle Q_{abs}. The length of the uncladded fiber z is replaced by the particle density N_s multiplied by the sensing surface area A_s (μm^2) since the total absorption depends on the number of particles adsorbed on the surface. A correction factor k is introduced to compensate for deviations from ideal assumptions, which will be discussed in more detail below. The final equation becomes the following:

$$A = \frac{4\sqrt{2}}{3V}\,(Q_{abs})(N_s)(A_s)(k) \tag{14}$$

Here, k is a dimensionless correction factor introduced to account for deviations from ideal assumptions in the combined model. Specifically, it captures geometric effects and particle–particle interactions not explicitly modeled, such as variations in nanoparticle spacing, partial monolayer coverage, and deviations from ideal random sequential adsorption (RSA) behavior. These effects are further explored in the next section, where the

dependence of absorbance on particle density and spacing is investigated. In this work, k is treated as a constant empirically chosen to match simulation trends and maintain consistency between analytical and numerical results. Its inclusion improves the model's fidelity while keeping the formulation tractable. It should be noted that since the sensor is evanescent wave-based, Equation (14) is a function of the absorption of the nanoparticle only, not the total extinction of the particle as shown by Sai et al. [31].

2.4. Combined Model Results

From the modeling results shown previously, it can be concluded that using 30 nm nanoparticles could result in a significantly higher absorption in the LSPR signal due to their larger absorption coefficient, and higher surface density when compared to 80 nm nanoparticles. The total absorbance as a result of the LSPR effect during adsorption can be obtained by combining Equations (5) and (14). Figure 6 shows the modeled LSPR absorption spectra as a function of wavelength using 30 nm and 80 nm nanoparticles in a medium such as water, which has a refractive index equal to 1.34.

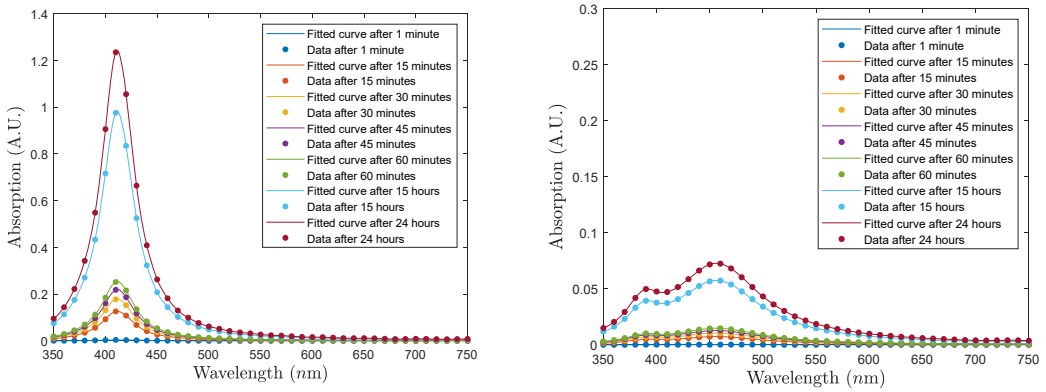


Figure 6. Modeled FOEW LSPR absorption spectra obtained from the combined model for sensors using (**a**) 30 nm and (**b**) 80 nm silver nanoparticles. Simulation results are interpolated using a cubic spline to demonstrate nanoparticle-size-dependent LSPR behavior on the fiber optic signal.

It can be observed from the results that the absorbance increases over time as the number of particles adsorbed on the surface increases. Additionally, the change in the LSPR absorbance suggests faster adsorption initially, with a significant decrease in adsorption as the surface density increases. This is expected since, according to the numerical absorption model of nanoparticles, the absorption increases proportionally with the number of particles, and according to the diffusion transport process adsorption model, the number of particles adsorbed on the surface of the fiber increases at a rate proportional to $\sqrt{t}$. Thus, the final absorption signal of the combined model is also increasing at a rate proportional to $\sqrt{t}$.

Three key limitations of this model should be noted. First, it does not account for the effects of repulsive forces on the adsorption rate after the formation of the monolayer. As a result, the model continues to show an increase in the adsorption signal for the entire duration of the simulation, which explains the significant rise observed between the 60-min mark and the 15-h mark.

Second, the model assumes that particles are separated by distances greater than their diameters, as was described in the nanoparticle–light interaction section. In practice, however, this assumption does not hold, as the adsorption process is random and often results in particles being in close proximity on the surface. Closer spacing between particles leads to well-documented plasmonic coupling effects, including a red shift in the peak

absorption wavelength and a broadening of the LSPR signal across multiple wavelengths. This occurs because, as particles get closer, their dipole fields begin to interact. As a result, the effective plasma frequency decreases, and the particles start resonating collectively as one larger, non-spherical structure [20]. This effect cannot be controlled by the fabrication process presented in this work. Moreover, the magnitude of the LSPR absorbance is also affected by the spacing. A lower quantity of particles with optimized distribution may result in a higher LSPR signal compared to a sensor with a higher quantity of particles with significant aggregation.

Finally, according to the RSA model, the maximum achievable surface coverage for spherical, non-charged nanoparticles is 0.547. However, silver nanoparticles are influenced by the electric double layer and zeta potential, which limit their maximum surface coverage. RSA can be used to estimate surface coverage, but not aggregation, since aggregation is governed by additional stochastic interactions. A more realistic prediction can be achieved by incorporating the effects of nanoparticle surface charge [29,30,40]. Nanoparticles with higher surface charge tend to adsorb more rapidly onto the surface but result in a lower monolayer density due to stronger repulsive forces. The surface coverage for non-charged spherical particles can be estimated using the following equation derived from the RSA model [43]:

$$\Theta = \pi \, r_{np}^2 \, N_s \tag{15}$$

The above-mentioned points are not captured in this model. This reinforces the need for the correction factor k in Equation (14) and highlights how it should be properly modeled to capture these effects. Nevertheless, these effects will be discussed further in the experimental results.

3. Fabrication Procedure

3.1. Materials

Standard Ø105 µm core glass clad silica multimode optical fiber, 0.22 NA, with 10 µm cladding (FG105LCA) and Ø125 µm coreless termination fiberglass rod (FG125LA) used to build the FOEW sensor were purchased from Thorlabs, USA. APTES ((3-Aminopropyl)-triethoxy-silane), (440140-100ML) was purchased from Sigma-Aldrich. Four aqueous-based colloidal solutions of spherical silver nanoparticles, 10 nm, 20 nm, 30 nm, and 80 nm in diameter (S-10-20, S-20-20, S-30-20, and S-80-20 respectively) were purchased from Cytodiagnostics®, Canada. The colloidal solutions were supplied in 2 mM sodium citrate, having a concentration of 20 PPM each.

3.2. FOEW LSPR Sensor Construction

Conventional fabrication of the sensing region in multimode fibers typically involves cladding etching with hydrofluoric acid to facilitate evanescent wave interaction with the surrounding medium [10]. However, this technique poses significant safety hazards, requires complex preparation steps, and often yields inconsistent results. In this study, a safer, time-efficient, and environmentally sustainable alternative was employed by using a coreless fiber as the sensing region. A coreless fiber is an optical fiber that does not have a distinct core region, and instead is made of pure silica. A 3.5 cm segment was prepared by manually stripping the protective coating and cutting the fiber to length using a precision fiber cleaver. This streamlined method enhances reproducibility, reduces health risks, and mitigates environmental impact. The processed coreless fiber was subsequently fusion-spliced to a standard multimode fiber, enabling effective evanescent field interaction with the external medium, creating the sensing region. A schematic representation of the fabricated FOEW LSPR sensor is shown in Figure 7.

Once the sensing region is prepared, the fiber is placed in an ultraviolet ozone treatment machine (UVO) for 10 min to clean the sensing region and increase the amount of Hydroxyl groups found on the surface. These groups are naturally found on the surface of glass but can be further increased via the use of UVO, through a process called surface hydroxylation [44]. Surface hydroxylation allows for higher APTES functionalization yield, resulting in improved nanoparticle adsorption and binding to the surface. UVO treatment optimizes this process by increasing the hydrophilicity of the surface by creating more OH-groups for APTES functionalization.

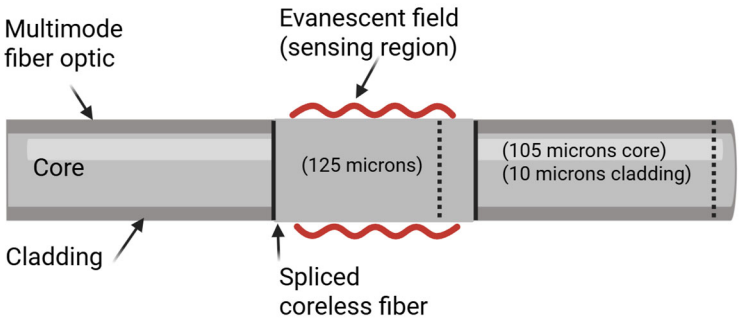


Figure 7. Schematic representation of the fabricated FOEW LSPR sensor, showing the integration of a coreless optical fiber section with a multimode fiber to form the sensing region.

Two FOEW sensors were prepared as described above to form the LSPR surface using different particle sizes (i.e., 80 nm and 30 nm silver nanoparticles). Salinization of the sensing region is then carried out by preparing a 1% APTES solution in DI water and allowing it to hydrolyze for more than 15 min. This breaks the saline groups via a process known as hydrolyzation. The sensing regions are then dipped in the 1% APTES solution for 30 min. The saline groups react with the hydroxyl groups on the glass surface, creating a covalent bond. Following this, the fibers are washed with DI water 3 times to remove any residual APTES molecules and dried under nitrogen for 2 min. The sensing region is then dipped in the nanoparticle solution for 15 h to provide sufficient time for the monolayer to form. A schematic highlighting the main fabrication steps is shown in Figure 8.

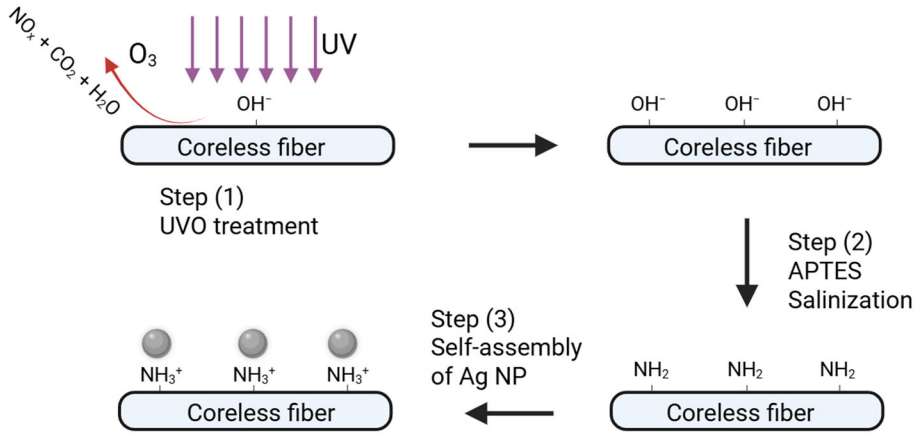


Figure 8. Step-by-step schematic of the FOEW LSPR sensor fabrication process, highlighting hydroxylation of the sensing region via UVO treatment, surface salinization via APTES functionalization, and silver nanoparticle self-assembly via adsorption.

The experimental setup schematic used to test the LSPR FOEW sensors, shown in Figure 9, was used. It consists of an Ocean Optics HL-2000-LL Light Source with wavelengths ranging from 360 nm to 2.4 µm, and an Ocean Optics USB 4000 spectrometer, with a response range from 200 nm to 1.1 µm. The spectrometer is connected to a computer and

Spectra suite software version 2.0.162 by Ocean Optics is used to record the absorption signal of the fiber in nanoparticle solution over the visible spectrum in real time. During testing, the sensor made using the 30 nm particles was connected to the light source and spectrometer as soon as it was dipped in the nanoparticle solution to monitor the signal and study the adsorption kinetics in real time. By contrast, the sensor made using 80 nm particles was not connected to the light source and spectrometer.

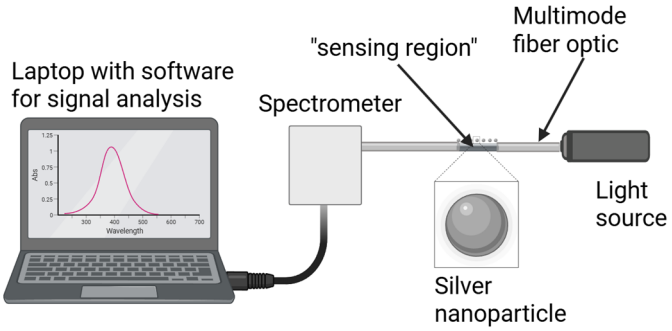


Figure 9. Experimental setup for FOEW LSPR measurements, including light source, sensor, and spectrometer arrangement used for capturing absorption spectra.

4. Results and Discussion

4.1. Combined Model Verification

The absorption signal was recorded every 15 min and is shown in Figure 10 for the 30 nm-based sensor. Initially, the LSPR peak was observed at 410 nm. However, as adsorption progressed, the peak gradually shifted to higher wavelengths, ultimately reaching 450 nm. As discussed in the combined model section, the experimental data reflects the effects of particle proximity, which were not accounted for in the theoretical model. As more nanoparticles adsorb onto the sensing region, their increasing proximity leads to electromagnetic coupling, altering each other's local fields. This interaction slows the LSPR oscillations, resulting in a red shift and a broader absorption peak, both of which are evident in the results. The recorded pattern in Figure 10 resembles the results obtained from the model displayed in Figure 6, further validating the combined model.

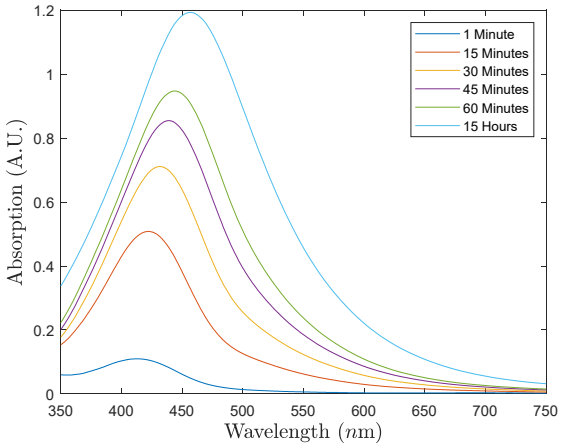
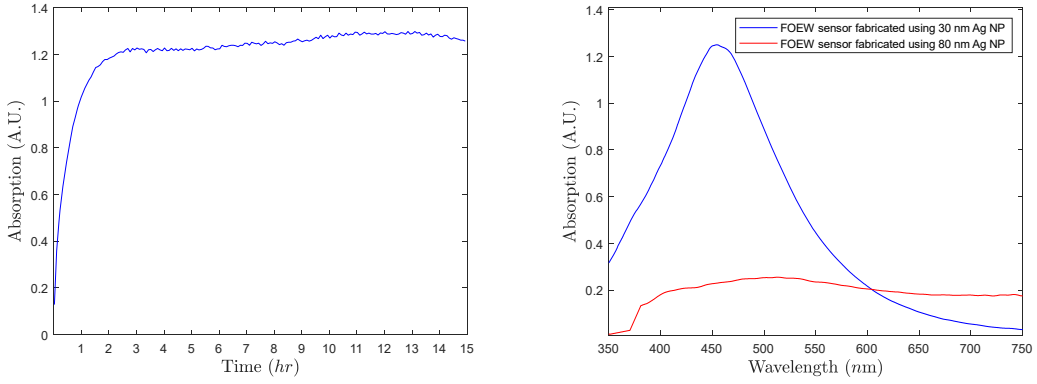


Figure 10. Time-resolved LSPR absorption signal collected during the adsorption process of 30 nm silver nanoparticles onto the coreless fiber surface, showing signal growth with increasing coverage.

The LSPR absorption magnitude measured over time for 30 nm nanoparticles is plotted in Figure 11a. The results show that the absorption signal reaches its maximum after approximately 5 h, indicating that maximum surface coverage has been achieved. The rate of adsorption was rapid during the first 2 h and slowed significantly between 2 and

3 h, consistent with the $\sqrt{t}$ dependence described in Section 2.4. The eventual plateau in the absorption signal after 5 h, an effect not captured by the theoretical model, suggests the formation of a complete monolayer. This also implies that repulsive forces, likely due to surface charge and the electric double layer, began to dominate, preventing further adsorption on the sensing region.



(**a**) (**b**)

Figure 11. (**a**) Temporal evolution of LSPR peak absorption magnitude for the 30 nm nanoparticle sensor during adsorption; (**b**) comparison of final absorption signals for sensors with 30 nm vs. 80 nm nanoparticles after 15 h of adsorption.

The LSPR signals from both sensors, those based on 30 nm and 80 nm silver nanoparticles, after 15 h of adsorption, are shown in Figure 11b. The sensor fabricated using 30 nm nanoparticles exhibits a clear and distinct peak around 450 nm, indicating strong localized surface plasmon resonance. In contrast, the sensor based on 80 nm nanoparticles does not show a well-defined peak. While a slight rise in absorbance is observable around 510 nm, the signal is broadly distributed across a wide wavelength range. This observation aligns with simulation results, which predicted that 80 nm silver nanoparticles produce significantly lower LSPR absorbance compared to their 30 nm counterparts. Furthermore, as discussed previously, the adsorption of larger nanoparticles leads to lower surface coverage due to their larger size, contributing to the weaker and broader LSPR signal observed in the 80 nm case.

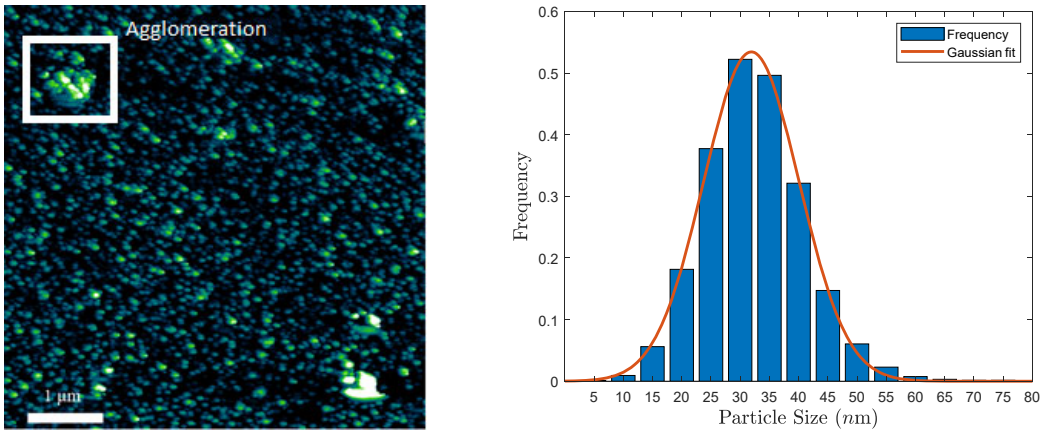
4.1.1. AFM Characterization

Atomic force microscopy (AFM) was employed to characterize the surface morphology of the sensors following the fabrication process. According to the adsorption model, a higher nanoparticle surface density and coverage are expected on the sensor fabricated using 30 nm silver nanoparticles compared to that fabricated with 80 nm nanoparticles. This is due to the smaller size of the 30 nm particles, which allows for a greater number to adsorb within the same surface area. The AFM images and analysis provided in Figures 12 and 13 confirm this expectation.

A comparison of the AFM results reveals distinct differences between the two sensors. For the sensor fabricated with 30 nm nanoparticles, the images consistently show a high surface density and well-dispersed nanoparticle coverage, indicating the formation of a uniform monolayer. In contrast, the 80 nm-based sensor exhibits significantly lower nanoparticle density and surface coverage. This trend was observed consistently across multiple AFM scans, reinforcing the validity of the adsorption model. While every image of the 30 nm-based sensor showed dense nanoparticle coverage, the 80 nm-based sensor repeatedly lacked similar features.

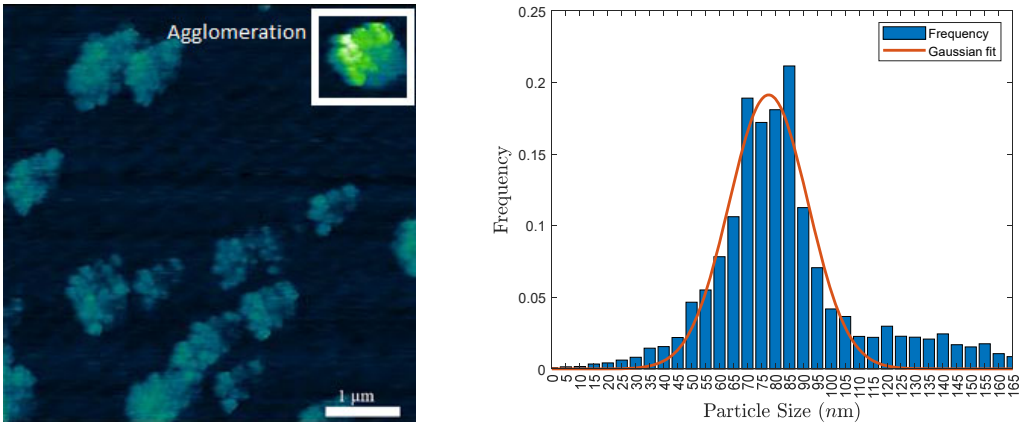
An additional observation is the relatively minor agglomeration present in the 30 nm-based sensor compared to the more pronounced clustering seen in the 80 nm-

based sensor. This could be attributed to the stronger van der Waals attractive forces between larger particles, which increase with mass and size. In contrast, the Coulomb repulsion between smaller, highly charged nanoparticles appears to be more effective in preventing aggregation, leading to better dispersion on the surface [45].



(**a**) (**b**)

Figure 12. (**a**) AFM image of the sensing region coated with 30 nm silver nanoparticles; (**b**) corresponding particle size frequency distribution derived from AFM analysis, indicating uniform nanoparticle distribution.



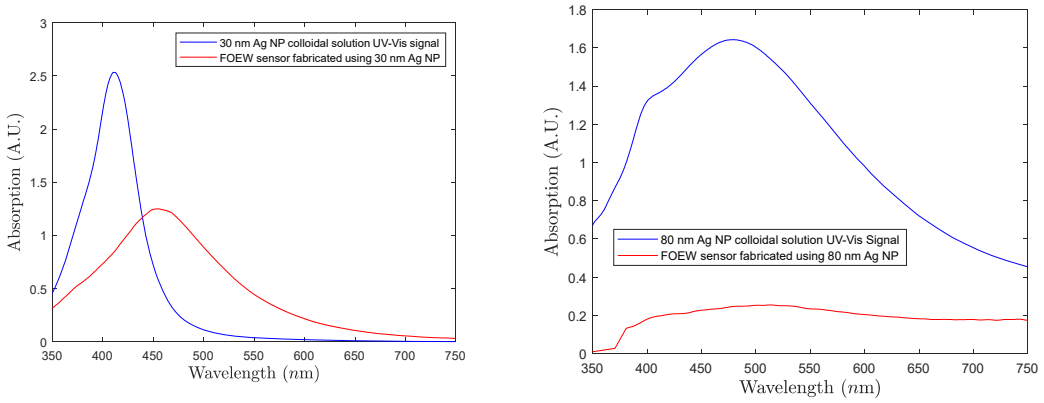
(**a**) (**b**)

Figure 13. (**a**) AFM image of the sensing region after 80 nm silver nanoparticle adsorption; (**b**) frequency distribution of nanoparticle size and surface density, showing reduced coverage and increased agglomeration compared to 30 nm nanoparticles.

4.1.2. UV–VIS Characterization

UV–VIS characterization measures the total light extinction resulting from both scattering and absorption, based on the particle cross-section. However, as previously discussed, FOEW sensors are primarily influenced by the absorption component of the medium. To confirm this, UV–VIS spectroscopy was performed on 30 nm and 80 nm silver nanoparticle solutions, and the resulting LSPR spectra were compared to those obtained from the corresponding FOEW sensors. Figure 14a presents the comparison between the 30 nm-based FOEW sensor and the UV–VIS spectrum of the 30 nm nanoparticle solution. The results show a clear difference between the two measurements. The LSPR peak observed in the FOEW sensor is red-shifted and broader compared to the UV–VIS spectrum. This discrepancy is due to nanoparticle adsorption and proximity effects on the fiber surface in the FOEW sensor, as discussed previously. In contrast, nanoparticles in the UV–VIS

solution are freely suspended and well-separated due to electrostatic repulsion, preventing such interactions and resulting in a sharper, unshifted LSPR peak.



(**a**) (**b**)

Figure 14. Comparison of LSPR spectra for (**a**) 30 nm silver nanoparticles and (**b**) 80 nm silver nanoparticles obtained via conventional UV–VIS spectroscopy and FOEW evanescent wave absorption. The results highlight that FOEW signal generation is predominantly governed by near-field absorption rather than by extinction, resulting in distinct spectral features compared to UV–VIS measurements.

The results comparing the 80 nm-based FOEW sensor to the UV–VIS spectrum of the 80 nm nanoparticle solution are shown in Figure 14b. Similar to the 30 nm case, a mismatch between the LSPR peak positions is observed. The FOEW sensor peak is red-shifted and broader relative to the UV–VIS measurement. The LSPR peaks for the 80 nm particles occur at longer wavelengths compared to the 30 nm particles, which is expected due to the increased particle size. However, a key observation is the significantly lower ratio of the FOEW absorption signal relative to the UV–VIS signal for the 80 nm particles, when compared to the 30 nm case. This can be explained by two factors: first, the total absorption efficiency of 80 nm nanoparticles is inherently lower in the FOEW configuration; second, their final surface density on the fiber is significantly reduced, as previously discussed.

In the UV–VIS measurements, the LSPR response arises from the total extinction cross-section, which includes both absorption and scattering. For 30 nm nanoparticles, the extinction is primarily driven by absorption, while for 80 nm nanoparticles, scattering dominates the response. These results support the predictions of the nanoparticle–light interaction model, and further confirm that 30 nm particles are more suitable for FOEW-based LSPR sensing due to their higher absorption efficiency. Therefore, evaluating nanoparticle performance based solely on extinction efficiency can be misleading for FOEW sensor applications. Instead, nanoparticles with a high absorption-to-extinction ratio should be selected for optimal sensor performance.

4.2. Studying the Effect of Higher Surface Density on FOEW LSPR Signal Enhancement

Referring to Figure 3, Figure 4, and Figure 5b, it can be argued that although 10 nm and 20 nm silver nanoparticles exhibit lower individual LSPR absorption compared to 30 nm nanoparticles, their smaller size could enable a higher packing density on the fiber surface. This increased surface coverage might lead to a higher overall LSPR signal from the sensor. To evaluate this hypothesis, three FOEW sensors were fabricated using 10 nm, 20 nm, and 30 nm silver nanoparticles, following the procedure outlined in the fabrication section. During the adsorption process, each sensor was connected to the light source and spectrometer to monitor the LSPR signal in real time. The resulting absorption spectra for each nanoparticle size are presented in Figure 15.

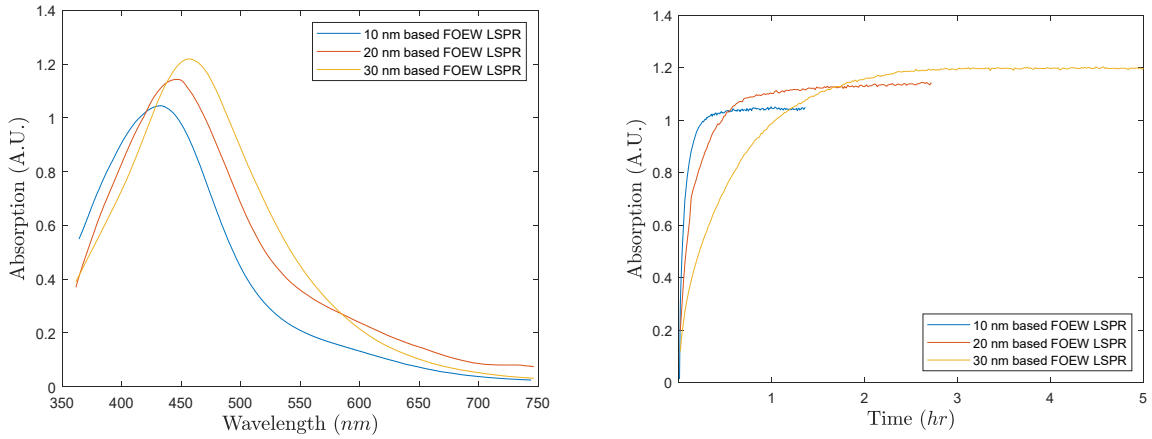


Figure 15. (**a**) Absorption spectra vs. wavelength for sensors fabricated with 10 nm, 20 nm, and 30 nm silver nanoparticles after adsorption completion; (**b**) corresponding LSPR peak intensity vs. time, highlighting the higher adsorption rate for smaller sizes.

Figure 15b provides critical insights into the adsorption kinetics, indicating that the self-assembly rate is inversely related to nanoparticle size. This behavior aligns with the theoretical diffusion-limited transport model presented earlier in this work and can be attributed to the higher surface-area-to-volume ratio of smaller nanoparticles, which enhances their diffusivity and promotes faster adsorption onto the sensing surface.

During the transient phase of adsorption, sensors employing smaller nanoparticles (10 nm and 20 nm) demonstrated higher absorption signals than the 30 nm-based sensors for equivalent fabrication durations. This is explained by the ability of smaller nanoparticles to achieve a higher surface density, resulting in a more pronounced cumulative optical response in the early stages of adsorption. These findings support the conclusion that nanoparticle size significantly influences both adsorption kinetics and optical signal development.

However, upon the formation of the monolayer, the trend reverses. Despite the lower particle density, the sensor fabricated with 30 nm nanoparticles exhibited the highest steady-state absorption signal. This can be attributed to the greater absorption efficiency of the 30 nm nanoparticles, which compensates for their reduced density on the sensor surface.

4.2.1. SEM Characterization

SEM images and analysis showing the final surface density and nanoparticle count are shown in Figure 16, where it is demonstrated how the smaller nanoparticles result in a significantly higher final surface density.

4.2.2. Refractive Index Sensitivity Testing

Smaller nanoparticles enhance adsorption kinetics and produce stronger transient absorption signals, whereas nanoparticles with higher absorption coefficients yield stronger final absorption signals due to their intrinsic optical properties. This balance between nanoparticle size and optical performance is critical for optimizing LSPR-based sensors for specific applications. However, a higher signal intensity does not directly correlate with improved sensor sensitivity, which requires further evaluation.

Refractive index (RI) sensitivity testing is essential for assessing the performance of FOEW LSPR sensors. This test measures the sensor's ability to detect small changes in refractive index, directly impacting its precision and reliability. The sensitivity was evaluated by measuring the LSPR wavelength shifts in media with varying refractive indices. A

glycerol/DI water dilution series was prepared with varying ratios of $V_{glycerol}/V_{DI\ water}$ of 0, 0.2, 0.4, 0.6, and 0.8. The values were obtained from [46] and are shown in Table 1.

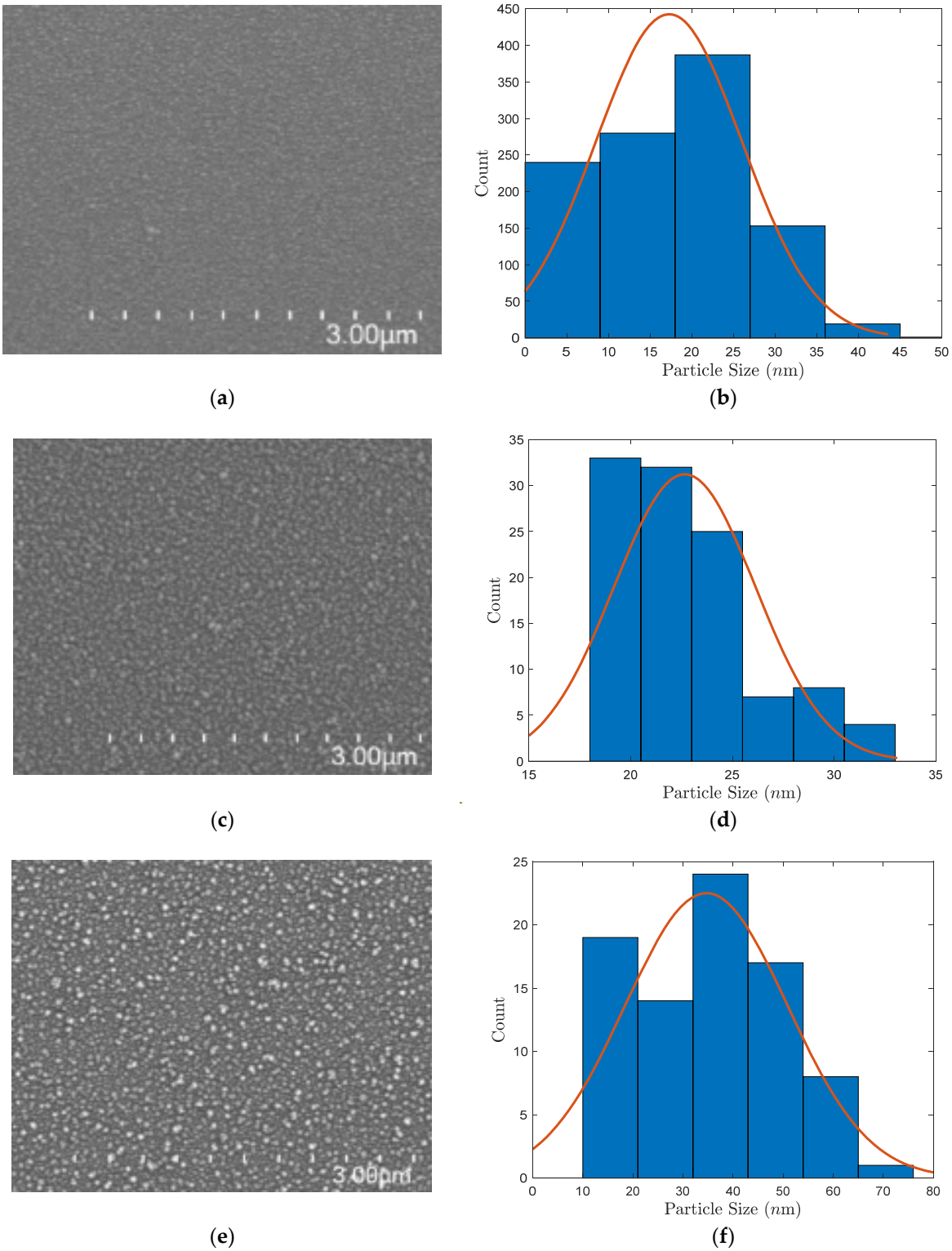


Figure 16. SEM images of fiber surfaces with adsorbed silver nanoparticles: (**a**) 10 nm, (**c**) 20 nm, (**e**) 30 nm; and corresponding surface density histograms in count per μm^2: (**b**), (**d**), and (**f**). The images highlight how nanoparticle size influences surface coverage and distribution, directly impacting the LSPR sensor's optical response.

Table 1. RI values of a dilution series of glycerol and DI water.

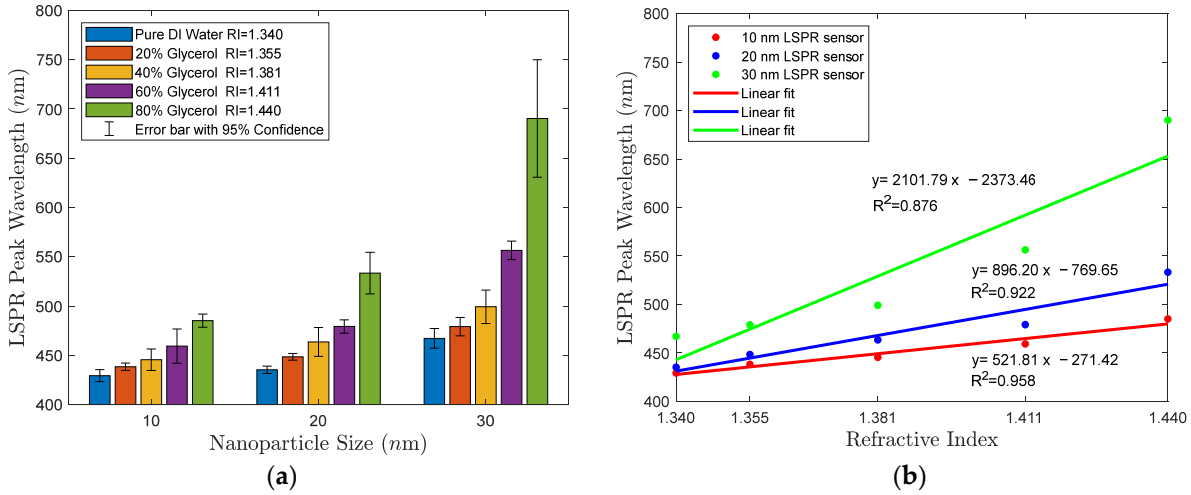
Volume Percentage Glycerol/DI Water	Refractive Index
0%	1.34
20%	1.355
40%	1.381
60%	1.411
80%	1.440

Three FOEW LSPR sensors, each incorporating nanoparticles of a specific size (10 nm, 20 nm, and 30 nm), were fabricated following the previously outlined method. Particles larger than 30 nm have lower absorption efficiencies, and result in lower final surface densities. Thus, they were not included in this study. Additionally, to preserve total internal reflection (TIR) within the fiber, only solutions with refractive indices up to 1.44 were considered. This upper limit was chosen because the sensing region of the FOEW structure has a refractive index of approximately 1.455; exceeding this value would compromise the TIR condition, thereby affecting the evanescent field and overall sensor performance.

To ensure accuracy, each measurement was performed three times for each sensor. The LSPR peak wavelength was recorded after the sensing region was fully immersed in solutions with varying refractive indices, and prepared using a glycerol dilution series. Between measurements, the sensing region was thoroughly washed with deionized (DI) water to restore the baseline and ensure consistent results. The sensitivity of the sensor (S) was calculated using the following equation:

$$S = \frac{\Delta\lambda_{LSPR}}{\Delta n} \tag{16}$$

where $\Delta\lambda_{LSPR}$ is the change of LSPR peak absorption in different media in (nm), and Δn is the change in the refractive index of the medium. This approach allows for a systematic evaluation of the refractive index sensitivity of each sensor, providing insights into the effect of nanoparticle size on sensor performance. The results are shown in Figure 17.



(**a**) (**b**)

Figure 17. Refractive index (RI) sensitivity results of FOEW LSPR sensors: (**a**) variation in LSPR peak shift for sensors fabricated with 10 nm, 20 nm, and 30 nm silver nanoparticles; (**b**) LSPR peak wavelength as a function of surrounding RI for each nanoparticle size, confirming the highest sensitivity for sensors using 30 nm silver nanoparticles.

Figure 17a illustrates that sensors fabricated using 30 nm nanoparticles exhibit significantly higher sensitivity to changes in the refractive index of the surrounding medium

compared to those utilizing 20 nm and 10 nm nanoparticles. As the refractive index of the medium increases, the LSPR peak wavelength of the 30 nm-based sensors undergoes a more substantial shift. To determine the RI sensitivity slopes and linearity (R^2) values, a first-order polynomial regression (linear fit) was applied to the mean LSPR peak positions obtained for each nanoparticle size (10, 20, and 30 nm) across the different refractive index values. The slope of the resulting linear fit corresponds to the RI sensitivity, while the coefficient of determination (R^2) was computed using the standard formula:

$$R^2 = 1 - \frac{SS_{res}}{SS_{tot}} \tag{17}$$

where SS_{res} and SS_{tot} represent the residual and total sum of squares, respectively. In addition, 95% confidence intervals were calculated for each data point using the standard error of the mean (SEM), derived from three repeated measurements, and multiplied by the 1.96 z-score for normal distributions. As shown in Figure 17b, the sensitivity of the 30 nm-based sensors was measured at 2101.79 nm/RIU, significantly outperforming the 20 nm-based sensors at 896.20 nm/RIU and the 10 nm-based sensors at 521.81 nm/RIU. This enhanced sensitivity can be attributed to the greater absorption efficiency associated with the 30 nm nanoparticles. These results are consistent with our theoretical expectations and exceed the typical sensitivity range reported for comparable nanoparticle-based FOEW sensors in the literature (78–989 nm/RIU) [47–49], approaching values generally observed only in more complex SPR/LSPR sensor configurations (up to 2161 nm/RIU) [50–52].

However, the linearity of the sensors, represented by the R^2 value, varied inversely with nanoparticle size. The 10 nm-based sensors demonstrated the highest linearity (R^2 = 0.958), followed by the 20 nm-based sensors (R^2 = 0.922) and the 30 nm-based sensors (R^2 = 0.876). This improved linearity for the 10 nm-based sensors may be attributed to a more uniform monolayer of nanoparticles and reduced aggregation during the fabrication process, thereby ensuring a more consistent and predictable sensing response. The error bars in Figure 17b are the same as those shown in Figure 17a, but were omitted for clarity.

5. Conclusions

In this study, we present a novel analysis to optimize the performance of FOEW LSPR sensors, emphasizing the unique nature of the evanescent field as a standing wave that interacts exclusively with absorbing media via their absorption coefficient, and is not affected by scattering. This intrinsic property distinguishes FOEW sensors from propagating wave systems, necessitating a shift from conventional optimization based on nanoparticles' extinction coefficients to a novel, absorption-driven design approach. Building upon classical ATR models in multimode fibers, we adapted the analytical foundation to describe the unique interaction of evanescent waves with silver nanoparticles. This adaptation incorporates nanoparticle-specific parameters such as absorption efficiency, surface density, and sensing surface area, enabling precise modeling of the FOEW LSPR absorption signal. Modeling and experimental analyses revealed that 30 nm silver nanoparticles deliver superior performance due to their higher absorption efficiency, reduced agglomeration, and enhanced coupling with the evanescent field.

By applying a diffusion transport model to describe nanoparticle adsorption kinetics, we optimized surface coverage as a function of nanoparticle size to maximize the LSPR absorption signal. Although 30 nm silver nanoparticles demonstrated the highest individual absorption efficiency, smaller nanoparticles were also investigated to assess whether their higher achievable surface densities could improve overall sensor performance. FOEW LSPR sensors fabricated with 10 nm, 20 nm, and 30 nm silver nanoparticles were subjected

to refractive index (RI) sensitivity testing. The results showed that, once monolayer coverage was achieved, the sensors incorporating 30 nm nanoparticles yielded the highest RI sensitivity at 2101.79 nm/RIU, significantly outperforming those fabricated with 20 nm (896.199 nm/RIU) and 10 nm (521.808 nm/RIU) particles and outperforms FOEW LSPR sensors fabricated similarly found in the literature. This superior performance is attributed to the enhanced absorption efficiency and more effective coupling with the evanescent field exhibited by the 30 nm nanoparticles.

Our work introduces a scalable, environmentally friendly fabrication method that leverages coreless fibers, surface functionalization via UVO treatment, and the self-assembly of silver nanoparticles. Unlike traditional surface preparation methods, which often involve hazardous chemicals, our approach is safer, more sustainable, and adaptable to large-scale production. The framework introduced in this work can be applied to various plasmonic materials, such as gold and copper, as well as different nanoparticle sizes, to identify the optimal configuration for light absorption. This provides a flexible platform for designing FOEW LSPR sensors and highlights the potential of absorption-driven design in improving FOEW LSPR sensor performance. It opens new possibilities for enhancing the sensitivity, reliability, and versatility of these sensors across a broad range of fields.

In real-world applications, this optimized FOEW LSPR sensor design can significantly enhance biosensing and chemical monitoring performance. For instance, the increased RI sensitivity and strong absorption response of the 30 nm silver nanoparticle-based sensors would allow for highly accurate detection of minute concentration changes, suitable for biosensing applications where biomarker concentrations are low, such as in saliva. Notably, the achieved sensitivity approach levels are typically reported only for more complex sensor configurations, despite the simplicity of the design and fabrication. The scalable, label-free fabrication approach also makes it well-suited for integration into portable, non-invasive diagnostic platforms and environmental monitoring systems.

Author Contributions: O.A. designed the modeling and experimental procedure; O.A. conducted the numerical and analytical modeling, ran the experiments, collected the data, compiled and analyzed the results, and prepared the manuscript with input from A.G. and P.N.; O.A. and A.G. were involved in the initial conception of the project, including idea generation, experimental design, data analysis and manuscript review; P.N. supervised the work, analyzed the data, and reviewed and corrected the manuscript. All authors have read and agreed to the published version of the manuscript.

Funding: This research is funded by the University of Waterloo Engineering Excellence Fellowship (EEF-D). The authors would like to acknowledge CMC Microsystems, manager of the FABrIC project funded by the Government of Canada, for the provision of products and services that facilitated this research. (www.cmc.ca), and ANSYS, including CAD tools.

Data Availability Statement: The data presented in this study are available on request from the corresponding author due to privacy reasons.

Acknowledgments: Figure 7, Figure 8, and Figure 9 were created with www.BioRender.com.

Conflicts of Interest: The authors declare no conflicts of interest.

Abbreviations

The following abbreviations are used in this manuscript:

FOEW	Fiber Optic Evanescent Wave
LSPR	Localized Surface Plasmon Resonance
AFM	Atomic Force Microscopy
SEM	Scanning Electron Microscopy
RI	Refractive Index

TIR	Total Internal Reflection
ATR	Attenuated Total Reflection
LOD	Limit of Detection
RSC	Reflectance Spectral Correction
ESD	Extinction Spectral Decomposition
APTES	(3-Aminopropyl)-tri-ethoxy-silane

References

1. Sadeque, M.S.B.; Chowdhury, H.K.; Rafique, M.; Durmuş, M.A.; Ahmed, M.K.; Hasan, M.M.; Erbaş, A.; Sarpkaya, İ.; Inci, F.; Ordu, M. Hydrogel-Integrated Optical Fiber Sensors and Their Applications: A Comprehensive Review. *J. Mater. Chem. C* **2023**, *11*, 9383–9424. [CrossRef]
2. Sharma, A.K.; Gupta, J.; Sharma, I. Fiber Optic Evanescent Wave Absorption-Based Sensors: A Detailed Review of Advancements in the Last Decade (2007–18). *Optik* **2019**, *183*, 1008–1025. [CrossRef]
3. Elsherif, M.; Alam, F.; Salih, A.E.; Wang, X.; Corridon, P.R.; Ramadi, K.B.; Butt, H. Fiber-Optic Probes for Real-Time pH Monitoring. *Sens. Diagn.* **2024**, *3*, 827–838. [CrossRef]
4. Zhang, H.; Zhou, X.; Li, X.; Gong, P.; Zhang, Y.; Zhao, Y. Recent Advancements of LSPR Fiber-Optic Biosensing: Combination Methods, Structure, and Prospects. *Biosensors* **2023**, *13*, 405. [CrossRef] [PubMed]
5. de Fornel, F. *Evanescent Waves: From Newtonian Optics to Atomic Optics*; Springer Science & Business Media: Berlin/Heidelberg, Germany, 2001; ISBN 978-3-540-65845-0.
6. Bertolotti, M.; Sibilia, C.; Guzman, A.M. *Evanescent Waves in Optics: An Introduction to Plasmonics*; Springer Series in Optical Sciences; Springer International Publishing: Cham, Switzerland, 2017; Volume 206, ISBN 978-3-319-61260-7.
7. Wang, P.; Brambilla, G.; Ding, M.; Semenova, Y.; Wu, Q.; Farrell, G. High-Sensitivity, Evanescent Field Refractometric Sensor Based on a Tapered, Multimode Fiber Interference. *Opt. Lett.* **2011**, *36*, 2233–2235. [CrossRef]
8. Khijwania, S.K.; Gupta, B.D. Fiber Optic Evanescent Field Absorption Sensor with High Sensitivity and Linear Dynamic Range. *Opt. Commun.* **1998**, *152*, 259–262. [CrossRef]
9. Satija, J.; Punjabi, N.S.; Sai, V.V.R.; Mukherji, S. Optimal Design for U-Bent Fiber-Optic LSPR Sensor Probes. *Plasmonics* **2014**, *9*, 251–260. [CrossRef]
10. Ghannoum, A.; Nieva, P.; Yu, A.; Khajepour, A. Development of Embedded Fiber-Optic Evanescent Wave Sensors for Optical Characterization of Graphite Anodes in Lithium-Ion Batteries. *ACS Appl. Mater. Interfaces* **2017**, *9*, 41284–41290. [CrossRef]
11. Xin, X.; Zhong, N.; Liao, Q.; Cen, Y.; Wu, R.; Wang, Z. High-Sensitivity Four-Layer Polymer Fiber-Optic Evanescent Wave Sensor. *Biosens. Bioelectron.* **2017**, *91*, 623–628. [CrossRef]
12. Zhong, N.; Zhao, M.; Zhong, L.; Liao, Q.; Zhu, X.; Luo, B.; Li, Y. A High-Sensitivity Fiber-Optic Evanescent Wave Sensor with a Three-Layer Structure Composed of Canada Balsam Doped with GeO_2. *Biosens. Bioelectron.* **2016**, *85*, 876–882. [CrossRef]
13. Chryssis, A.N.; Lee, S.M.; Lee, S.B.; Saini, S.S.; Dagenais, M. High Sensitivity Evanescent Field Fiber Bragg Grating Sensor. *IEEE Photonics Technol. Lett.* **2005**, *17*, 1253–1255. [CrossRef]
14. Hammond, J.L.; Bhalla, N.; Rafiee, S.D.; Estrela, P. Localized Surface Plasmon Resonance as a Biosensing Platform for Developing Countries. *Biosensors* **2014**, *4*, 172–188. [CrossRef]
15. Altug, H.; Oh, S.-H.; Maier, S.A.; Homola, J. Advances and Applications of Nanophotonic Biosensors. *Nat. Nanotechnol.* **2022**, *17*, 5–16. [CrossRef] [PubMed]
16. Unser, S.; Bruzas, I.; He, J.; Sagle, L. Localized Surface Plasmon Resonance Biosensing: Current Challenges and Approaches. *Sensors* **2015**, *15*, 15684–15716. [CrossRef]
17. Mao, Z.; Peng, X.; Zhou, Y.; Liu, Y.; Koh, K.; Chen, H. Review of Interface Modification Based on 2D Nanomaterials for Surface Plasmon Resonance Biosensors. *ACS Photonics* **2022**, *9*, 3807–3823. [CrossRef]
18. Kunwar, S.; Sui, M.; Pandey, P.; Gu, Z.; Pandit, S.; Lee, J. Improved Control on the Morphology and LSPR Properties of Plasmonic Pt NPs through Enhanced Solid State Dewetting by Using a Sacrificial Indium Layer. *RSC Adv.* **2019**, *9*, 2231–2243. [CrossRef]
19. Ohodnicki, P.R.; Buric, M.P.; Brown, T.D.; Matranga, C.; Wang, C.; Baltrus, J.; Andio, M. Plasmonic Nanocomposite Thin Film Enabled Fiber Optic Sensors for Simultaneous Gas and Temperature Sensing at Extreme Temperatures. *Nanoscale* **2013**, *5*, 9030–9039. [CrossRef] [PubMed]
20. Bohren, C.F.; Huffman, D.R. *Absorption and Scattering of Light by Small Particles*, 1st ed.; Wiley: Hoboken, NJ, USA, 1998; ISBN 978-0-471-29340-8.
21. Ha, J.W. Strategies for Sensitivity Improvement of Localized Surface Plasmon Resonance Sensors: Experimental and Mathematical Approaches in Plasmonic Gold Nanostructures. *Appl. Spectrosc. Rev.* **2022**, *58*, 346–365. [CrossRef]
22. Bin-Alam, M.S.; Reshef, O.; Mamchur, Y.; Alam, M.Z.; Carlow, G.; Upham, J.; Sullivan, B.T.; Ménard, J.-M.; Huttunen, M.J.; Boyd, R.W.; et al. Ultra-High-Q Resonances in Plasmonic Metasurfaces. *Nat. Commun.* **2021**, *12*, 974. [CrossRef]

23. Stankevičius, E.; Vilkevičius, K.; Gedvilas, M.; Bužavaitė-Vertelienė, E.; Selskis, A.; Balevičius, Z. Direct Laser Writing for the Formation of Large-Scale Gold Microbumps Arrays Generating Hybrid Lattice Plasmon Polaritons in Vis–NIR Range. *Adv. Opt. Mater.* **2021**, *9*, 2100027. [CrossRef]
24. Xu, T.; Geng, Z. Strategies to Improve Performances of LSPR Biosensing: Structure, Materials, and Interface Modification. *Biosens. Bioelectron.* **2021**, *174*, 112850. [CrossRef] [PubMed]
25. Lin, X.; Luo, Y.; Li, D.; Li, Y.; Gong, T.; Zhao, C.; Wang, C.; Duan, R.; Yue, W. Recent Advances in Localized Surface Plasmon Resonance (LSPR) Sensing Technologies. *Nanotechnology* **2025**, *36*, 202001. [CrossRef]
26. Jackman, J.A.; Ferhan, A.R.; Cho, N.-J. Nanoplasmonic Sensors for Biointerfacial Science. *Chem. Soc. Rev.* **2017**, *46*, 3615–3660. [CrossRef]
27. Rivero, P.J.; Goicoechea, J.; Arregui, F.J. Localized Surface Plasmon Resonance for Optical Fiber-Sensing Applications. In *Nanoplasmonics—Fundamentals and Applications*; Barbillon, G., Ed.; InTech: London, UK, 2017; ISBN 978-953-51-3277-6.
28. Milosevic, M. On the Nature of the Evanescent Wave. *Appl. Spectrosc.* **2013**, *67*, 126–131. [CrossRef]
29. Oćwieja, M.; Adamczyk, Z.; Morga, M.; Kubiak, K. Silver Particle Monolayers—Formation, Stability, Applications. *Adv. Colloid Interface Sci.* **2015**, *222*, 530–563. [CrossRef]
30. Oćwieja, M.; Adamczyk, Z.; Kubiak, K. Tuning Properties of Silver Particle Monolayers via Controlled Adsorption–Desorption Processes. *J. Colloid Interface Sci.* **2012**, *376*, 1–11. [CrossRef]
31. Sai, V.V.R.; Kundu, T.; Mukherji, S. Novel U-Bent Fiber Optic Probe for Localized Surface Plasmon Resonance Based Biosensor. *Biosens. Bioelectron.* **2009**, *24*, 2804–2809. [CrossRef] [PubMed]
32. Tu, M.H.; Sun, T.; Grattan, K.T.V. Optimization of Gold-Nanoparticle-Based Optical Fibre Surface Plasmon Resonance (SPR)-Based Sensors. *Sens. Actuators B Chem.* **2012**, *164*, 43–53. [CrossRef]
33. Lee, H.; Kim, H.-J.; Park, J.-H.; Jeong, D.H.; Lee, S.-K. Effects of Surface Density and Size of Gold Nanoparticles in a Fiber-Optic Localized Surface Plasmon Resonance Sensor and Its Application to Peptide Detection. *Meas. Sci. Technol.* **2010**, *21*, 085805. [CrossRef]
34. Habibi Masheli, M.; Eyvazi, S.; Aghdaee, M.; Amjad, J.M. LSPR of Nanoparticles Inside Strong Absorbent Medium. *J. Phys. Chem. C* **2023**, *127*, 23696–23705. [CrossRef]
35. Gérardy, J.M.; Ausloos, M. Absorption Spectrum of Clusters of Spheres from the General Solution of Maxwell's Equations. II. Optical Properties of Aggregated Metal Spheres. *Phys. Rev. B* **1982**, *25*, 4204–4229. [CrossRef]
36. Jiang, Y.; Pillai, S.; Green, M.A. Realistic Silver Optical Constants for Plasmonics. *Sci. Rep.* **2016**, *6*, 30605. [CrossRef] [PubMed]
37. Johnson, P.B.; Christy, R.W. Optical Constants of the Noble Metals. *Phys. Rev. B* **1972**, *6*, 4370–4379. [CrossRef]
38. Palik, E.D. *Handbook of Optical Constants of Solids*; Academic Press: Cambridge, MA, USA, 1998; ISBN 978-0-12-544423-1.
39. dos Santos, D.S., Jr.; Sanfelice, R.C.; Alvarez-Puebla, R.; Oliveira, O.N., Jr.; Aroca, R.F. Optical Enhancing Properties in Layer-by-Layer Films of Dendrimer and Gold Nanoparticles. *Macromol. Symp.* **2006**, *245–246*, 325–329. [CrossRef]
40. Morga, M.; Adamczyk, Z.; Oćwieja, M. Stability of Silver Nanoparticle Monolayers Determined by in Situ Streaming Potential Measurements. *J. Nanopart. Res.* **2013**, *15*, 2076. [CrossRef] [PubMed]
41. Ruddy, V.; MacCraith, B.D.; Murphy, J.A. Evanescent Wave Absorption Spectroscopy Using Multimode Fibers. *J. Appl. Phys.* **1990**, *67*, 6070–6074. [CrossRef]
42. *Sensing Technology: Current Status and Future Trends III*; Smart Sensors, Measurement and Instrumentation; Mason, A., Mukhopadhyay, S.C., Jayasundera, K.P., Eds.; Springer International Publishing: Cham, Switzerland, 2015; Volume 11, ISBN 978-3-319-10947-3.
43. Random Sequential Adsorption. *J. Theor. Biol.* **1980**, *87*, 237–254. [CrossRef]
44. Fan, Z.; Zhi, C.; Wu, L.; Zhang, P.; Feng, C.; Deng, L.; Yu, B.; Qian, L. UV/Ozone-Assisted Rapid Formation of High-Quality Tribological Self-Assembled Monolayer. *Coatings* **2019**, *9*, 762. [CrossRef]
45. Fine Particle—An Overview | ScienceDirect Topics. Available online: https://www-sciencedirect-com.proxy.lib.uwaterloo.ca/topics/materials-science/fine-particle (accessed on 15 June 2022).
46. Bochert, R. Contribution to Comprehension of Image Formation in Confocal Microscopy of Cornea with Rostock Cornea Module. *Br. J. Ophthalmol.* **2005**, *89*, 1351–1355. [CrossRef]
47. Sanders, M.; Lin, Y.; Wei, J.; Bono, T.; Lindquist, R.G. An Enhanced LSPR Fiber-Optic Nanoprobe for Ultrasensitive Detection of Protein Biomarkers. *Biosens. Bioelectron.* **2014**, *61*, 95–101. [CrossRef]
48. Csaki, A.; Jahn, F.; Latka, I.; Henkel, T.; Malsch, D.; Schneider, T.; Schröder, K.; Schuster, K.; Schwuchow, A.; Spittel, R.; et al. Nanoparticle Layer Deposition for Plasmonic Tuning of Microstructured Optical Fibers. *Small* **2010**, *6*, 2584–2589. [CrossRef] [PubMed]
49. Lu, M.; Zhu, H.; Lin, M.; Wang, F.; Hong, L.; Masson, J.-F.; Peng, W. Comparative Study of Block Copolymer-Templated Localized Surface Plasmon Resonance Optical Fiber Biosensors: CTAB or Citrate-Stabilized Gold Nanorods. *Sens. Actuators B Chem.* **2021**, *329*, 129094. [CrossRef]

50. Luo, Z.; Zhang, J.; Wang, Y.; Chen, J.; Li, Y.; Duan, Y. An Aptamer Based Method for Small Molecules Detection through Monitoring Salt-Induced AuNPs Aggregation and Surface Plasmon Resonance (SPR) Detection. *Sens. Actuators B Chem.* **2016**, *236*, 474–479. [CrossRef]
51. Feng, J.; Gao, J.; Yang, W.; Liu, R.; Shafi, M.; Zha, Z.; Liu, C.; Xu, S.; Ning, T.; Jiang, S. LSPR Optical Fiber Sensor Based on 3D Gold Nanoparticles with Monolayer Graphene as a Spacer. *Opt. Express* **2022**, *30*, 10187–10198. [CrossRef]
52. Jia, S.; Bian, C.; Sun, J.; Tong, J.; Xia, S. A Wavelength-Modulated Localized Surface Plasmon Resonance (LSPR) Optical Fiber Sensor for Sensitive Detection of Mercury(II) Ion by Gold Nanoparticles-DNA Conjugates. *Biosens. Bioelectron.* **2018**, *114*, 15–21. [CrossRef]

Disclaimer/Publisher's Note: The statements, opinions and data contained in all publications are solely those of the individual author(s) and contributor(s) and not of MDPI and/or the editor(s). MDPI and/or the editor(s) disclaim responsibility for any injury to people or property resulting from any ideas, methods, instructions or products referred to in the content.